Author's Accepted Manuscript

www.elsevier.com/locate/jssc

The structure of nano-palladium deposited on carbon-based supports

Ľubomír Pikna, Ondrej Milkovič, Karel Saksl, Mária Heželová, Miroslava Smrčová, Pavel Puliš, Štefan Michalik, Jana Gamcová

PII: S0022-4596(14)00036-X
DOI: http://dx.doi.org/10.1016/j.jssc.2014.01.032
Reference: YJSSC18348

To appear in: *Journal of Solid State Chemistry*

Received date: 3 July 2013
Revised date: 23 January 2014
Accepted date: 25 January 2014

Cite this article as: Ľubomír Pikna, Ondrej Milkovič, Karel Saksl, Mária Heželová, Miroslava Smrčová, Pavel Puliš, Štefan Michalik, Jana Gamcová, The structure of nano-palladium deposited on carbon-based supports, *Journal of Solid State Chemistry*, http://dx.doi.org/10.1016/j.jssc.2014.01.032

The structure of nano-palladium deposited on carbon-based supports.

Ľubomír Pikna[a*], *Ondrej Milkovič*[a], *Karel Saksl*[b], *Mária Heželová*[a], *Miroslava Smrčová*[a], *Pavel Puliš*[a], *Štefan Michalik*[c], *Jana Gamcová*[d]

[a]Faculty of Metallurgy, Technical University of Košice, Letná 9, 042 00 Košice, Slovakia, lubomir.pikna@tuke.sk, ondrej.milkovic@tuke.sk, maria.hezelova@tuke.sk, miroslava.smrcova@tuke.sk, pavel.pulis@tuke.sk,

[b]Institute of Materials Research, Slovak Academy of Sciences, Watsonova 47, 040 01 Košice, Slovakia, ksaksl@imr.saske.sk

[c]Institute of Physics, Faculty of Science, UPJŠ, Park Angelinum 9, 041 54 Košice, Slovakia, stefan.michalik@upjs.ke

[d]Deutsches Elektronen Synchrotron (DESY), Notkestraße 85, 22603 Hamburg, Germany, jana.gamcova@desy.de

---

* corresponding author: Ľubomír Pikna, e-mail: lubomir.pikna@tuke.sk, phone: +421-55-602-2300, fax: +421-55-602-2311, postal address: Faculty of Metallurgy, Technical University of Košice, Letná 9, 042 00 Košice, Slovakia

Keywords: nano-palladium, catalysts, structural analysis, activated carbon, carbon nanotubes

Abstract

Nano-palladium catalysts, prepared using the same procedure with the same metal content (3 wt. %) and two different supports, activated carbon (Pd/C) and activated carbon - multiwalled carbon nanotubes (Pd/C/CNT), are discussed. The simple technique of deposition reduction was applied in the preparation of these two types of Pd catalysts. TEM, XRD analysis, EXAFS signal analysis, and XANES were used for sample characterization. In both samples, transmission electron microscopy identified nanosized Pd particles with nearly spherical morphology but different sizes. The mean diameters of the particles on Pd/C and Pd/C/CNT were estimated to be 5.4 nm and 7.8 nm, respectively. The EXAFS signal analysis showed that Pd atoms on the particle surfaces were coordinated by 4 oxygens to form a PdO monolayer covering a metallic core. The XANES signal analysis indicated a smaller particle size for Pd/C (Ø 5 nm) than for Pd/C/CNT (Ø 10 nm), in good agreement with the TEM observations.

1 Introduction

Currently, catalysis plays an important role, especially in the field of fine chemicals. Supported catalysts have been successfully used in chemical industries for a long time, and they are still of special interest. High activity, selectivity and stability are the basic requirements of an effective catalyst that is useful for a specific application. Some of the conditions for high activity are a sufficiently large specific surface area (SSA) of the support, stability at relatively high temperatures and a high dispersion of the palladium particles [1].

Different types of materials [2-10] have been used as supports for palladium catalysts. It has been observed that carbon materials are stable in concentrated solutions of acids and bases, so they can be used as catalyst supports for a variety of applications.

Activated carbon (C) is one of the most common carriers used in the preparation of solid catalysts based on noble metals, particularly because of its chemical inertness, cost, large specific surface area and "recycling" - the recovery of the metal after the reaction. Its structure is complex and consists of macropores, mesopores and micropores [1,11]. Active carbon was used as the support for palladium in the hydrogenation of nitrobenzene to aniline in a liquid medium [12]. Even after the oxidization treatment of active carbon, a dispersion of 5 wt. % Pd impregnated on the support showed high activity.

In addition to activated carbon, carbon nanofibres (CNF) and/or carbon nanotubes (CNT) (either single-walled or multiwalled), are interesting catalyst supports mainly due to certain, specific characteristics, including the ability to control the porosity and surface chemistry [13]. These nanostructured materials were previously studied in depth for possible applications in catalysis [14-16]. The high purity of CNT and CNF can avoid catalyst self-poisoning. Moreover, the mesoporous nature of these supports can be of interest for liquid-phase reactions because it should allow for significantly decreased mass-transfer limitations compared with activated carbon.

Carbon nanofibres and carbon nanotubes were used as supports for Pt and Pd catalysts prepared using different loading methods, including the colloidal microwave process (CMP). The results indicated a strong influence of the carbon nanomaterials on the performance of the catalysts [17]. Ni and Pd particles supported by CNT showed excellent selective hydrogenation capacity for crotonaldehyde [18]. Zhang and co-authors [19] described Pd clusters as collecting in the interior of the multiwalled CNT. The results of liquid phase benzene hydrogenation

experiments exhibited higher catalytic activity than other supports, such as Y zeolite and activated carbon.

The aim of the present work is to report the synthesis and characterization of palladium - activated carbon (Pd/C) and palladium - activated carbon - multiwalled carbon nanotube (Pd/C/CNT) catalysts. Unlike other works that describe the preparation of catalysts on pure C or pure CNT as supports, this study is devoted to Pd loading on an unusual type of catalyst support, a mixture of C and CNT. The goal was to compare the structures of catalysts prepared in the same way with the same metal content (3 wt. %) using two different supports.

2 Experimental

2.1 Supports

Activated carbon (C) (NORIT® SX PLUS, Norit Americans Inc. USA), SSA 1100 $m^2 g^{-1}$, and multiwalled carbon nanotubes (CNT) (Chengdu organic chemicals Ltd., China), OD 10-20 nm, length 10-30 μm, purity 95+ %, and SSA 200 $m^2 g^{-1}$, were used as the support materials for Pd catalyst preparation. The specific surface areas of the supports were declared by the producers.

Before the CNT were applied, they were purified by refluxing in a mixture of concentrated nitric acid for 6 hours. After filtration and washing with distilled water to neutral pH, the nanotubes were dried at 105 °C to a constant weight.

2.2 Preparation of the catalyst

The simple technique of deposition reduction of palladium was applied [1]. It is based on the addition of a reducing agent to a suspension composed of the support material and a precursor of a noble metal. The reducing agent is responsible for the direct deposition of the metal onto the

support surface. This procedure is especially suitable for the production of noble metal supported catalysts because of their favorable reduction potentials.

The preparation of palladium on activated carbon (Pd/C) (3 wt. %) was realized through the addition of formaldehyde (the reducing agent) to a boiling suspension of the support in a solution of Na_2PdCl_4 at a pH value of 10-11. After an hour of exposure, the mixture was filtrated, rinsed with a sodium carbonate solution and dried to 40-60% wetness.

For the preparation of the Pd/C/CNT catalyst, a mixture of C and CNT at a weight ratio of 1:1 was used. The carbon nanotubes had to be suspended in a sodium carbonate solution using an ultrasound for 20 minutes. Then, the activated carbon was added, and a mixture of C and CNT was prepared. The Pd/C/CNT catalyst was prepared according to the procedure mentioned above.

2.3 Experimental methods

The specific surface area for the evaluated samples was determined using BET analysis on a high-speed gas sorption analyzer model NOVA 1000e (Quantachrome Instruments, USA). Nitrogen was used as the sorption gas.

Transmission electron microscopy (TEM) observations and selected area electron diffraction (SAED) were carried out using a JEOL JEM 2000 FX operated at 200 kV. The samples for the TEM observation were prepared through the ultrasonic dispersion of the powder samples in methanol and dropped on a carbon coated copper grid.

Hard X-ray diffraction measurements (XRD) were carried out at the BW5 experimental station [20] located at the DORIS III positron storage ring (energy 4.45 GeV, current 140–100 mA) at HASYLAB/DESY in Hamburg, Germany. The powder samples were poured on the top of a flat sample stage, and the sample was irradiated for 20 seconds by an incident beam of photons with

an energy of 100 keV (λ = 0.12398 Å) and a cross-section of 0.5 x 0.5 mm. The irradiation of the sample without a container ensures that the XRD patterns contain only the signal from the weakly scattering material and the inevitable air scattering and that the signal will be free of any container contributions. The resulting 2D XRD patterns were recorded using a Perkin Elmer 1621 detector. The collected data were then integrated into angular (2 Theta) space using the FIT2D software [21]. The sample-detector distance, the detector orthogonality with respect to the incoming radiation and the precise radiation energy were determined by fitting a standard reference CeO_2 sample.

X-ray absorption fine-structure (XAFS) measurements were performed at beamline X1 located at the same synchrotron storage ring. Spectroscopic data in the range of 24100 to 25100 eV were collected in transmission and fluorescence modes using a fixed-exit double-crystal Si (311) monochromator. During all XAFS measurements, the samples, encapsulated in a thin-walled, plastic container with an internal diameter of 10 mm, were irradiated by an X-ray beam with a cross-section of 4 x 1.5 mm (width x height). The X-ray intensities were monitored using ionization chambers filled with krypton gas at 100 mbar (10% absorption), 630 mbar (50% absorption) and 1 bar (100% absorption) for the first, second and third ionization chamber, respectively. The fluorescence detector (Passivated Implanted Planar Silicon, PIPS) was placed approximately 10 cm away from the sample and at an angle of 45^o with respect to the incoming X-ray beam. The energy calibration at the Pd-K edge was monitored by using a pure Pd thin foil as a reference material, measured at the same time as the sample. The experimentally measured X-ray absorption cross sections, μ(E)x, were analyzed using the FEFF 9.01 (program for ab initio multiple scattering calculations of the X-ray absorption fine structure) [22] and Viper (program for XAFS data processing and refinement) codes [23].

2.3.1 Near Edge X-ray Absorption Fine Structure (XANES) calculation

The near edge features (50–100 eV above the edge) reflect the local electron density of the states close to the Fermi level. This signal provides information about the local symmetry and local network topology. Therefore, XANES analysis could allow for the recovery of the detailed, 3D local structure around the absorber [24]. For the calculation of the X-ray absorption spectra, two theoretical methods are available: (1) the band structure theory [25] and (2) the real space multiple scattering (RSMS) theory [26,27]. FEFF represents the most commonly used software of the RSMS codes designed for XANES signal calculations for given atomic clusters [22]. In that code, a local structure around the absorber is assumed and, according to the muffin-tin approximation, the potential action of the photoelectron is calculated. The results are then used to solve the Schrödinger equation in the multiple-scattering formalism. Finally, the absorption cross section is evaluated. Good results were produced using this procedure in many different systems [28,29].

The qualitative comparison of the XANES signals at the Pd K-edge resulting from the Pd-based nanoparticles with the theory curves, calculated for Pd-metal cores coated with a PdO monolayer using the FEFF 9.01 program, is presented in the results of this paper.

2.3.2 Refinement of the local structure parameters from Extended X-ray Absorption Fine Structure (EXAFS)

EXAFS usually refers to the oscillating part of the XAFS signal between ~70 eV and 1000 eV above the absorption edge of a particular element of a sample. The signal contains structural information about the short range order around a specific type of atom, and its analysis provides a practical way to study the local atomic arrangement in materials.

The EXAFS signal, $\chi(k)$, measured above the Pd K-edge, was first extracted and weighted by k^2. The region in which the non-weighted amplitude of the oscillatory signal, $\chi(k)$, still

dominates over the noise (for details, see [23]) was Fourier transformed (*FT*) to real space. The obtained *FT* presents an equivalent to the pair correlation function, but its signal is modified by phase shifts due to the photoelectron emission and backscattering process. In the next step, the main peak from the *FT* was filtered (using a Hanning window function, 0-2.93 Å, coefficient A = 0.01) and back transformed to k-space.

To derive quantitative values for the interatomic distances, R, the coordination numbers, N, the mean-square relative displacements, σ^2, and the threshold energy shifts, E_o, a numerical curve fitting analysis of the k-space amplitudes and phases needs to be conducted by following the EXAFS formula based on a single-scattering approximation [30]:

$$k^2\chi(k) = k^2\sum_i C_i(k)\sin[2kR_i + \varphi_i(k)] \qquad (1)$$

The summation extends over *i* coordination shells at an average distance R_i from the absorbing atom. $\varphi_i(k)$ is the total phase shift due to the contribution from both the absorbing and back-scattering atom, and *k* is the photoelectron wave vector. The conversion between the wave vector and the energy is $k = \sqrt{\frac{2m}{\hbar^2}(E - E_o)}$. Here, *m* is the mass of an electron, $\hbar = \frac{h}{2\pi}$ is Planck's constant, *E* is the incident photon energy and E_o is the threshold energy of that particular absorption edge. The amplitude factor $C_i(k)$ is given by

$$C_i(k) = \frac{N_i}{kR_i^2} S_0^2 F_i(k) \exp(-2\sigma_i^2 k^2) \qquad (2)$$

where N_i is the average number of scattering atoms (coordination number), S_0^2 is an energy-independent many-body amplitude reduction factor that accounts for losses only within the central absorbing atom and is independent of the chemical nature and type of back-scattering atoms, $F_i(k)$ is the backscattering amplitude characteristic of a particular type of back-scattering

atom and σ_i^2 is the mean square relative displacement. Expressions (1) and (2) are implemented in the program Viper for EXAFS data processing and refinement. The back-scattering amplitude $F_i(k)$, the phase shift $\varphi_i(k)$ and the many-body amplitude reduction factors, S_0^2, were calculated from the provided atomic configuration using the FEFF 9.01 code.

3 Results and discussion

The specific surface area of the catalyst is an important characteristic because of its impact on the final activity and selectivity in the process of heterogeneous catalysis. Therefore, the surface areas of the supports and prepared catalysts were observed as the outputs of single-point BET analysis.

Measured SSA values of support materials were 890 $m^2 g^{-1}$ for activated carbon (C), 167 $m^2 g^{-1}$ for carbon nanotubes (CNT), and 550 $m^2 g^{-1}$ for the C/CNT mixture. The results for C and CNT supports are slightly different from the values declared by the producers.

The SSA values of prepared catalysts were 692 $m^2 g^{-1}$ for Pd/C and 531 $m^2 g^{-1}$ for Pd/C/CNT. Palladium loaded onto the support caused pore blocking, which resulted in a decrease of the specific surface area of the prepared catalysts. The lower value of SSA in Pd/C/CNT is a result of the mixing of the support materials.

3.1 Transmission electron microscopy

Figure 1a shows the TEM observation of the Pd/C specimen. In the bright field on the activated carbon surface, the nanosized Pd particles were identified. The SAED sample pattern shown in Figure 2a demonstrates that nanoparticles have lattice parameters very similar to the pure Pd with face centered cubic (FCC) unit cell (space group Fm-3m). The observation of the Pd/C/CNT specimen shows similar nanoparticles with a difference in the carbon substrate, consistent with activated carbon powder particles wrapped around the CNT (Figure 1b). The particles in both samples exhibit nearly spherical morphology but different sizes. The mean diameters of the particles in the Pd/C and Pd/C/CNT samples were estimated to be 5.4 nm and 7.8 nm, respectively. A Pd particle size distribution histogram from over 200 particles analyzed for each sample is shown in Figure 3.

The nanoparticle compositions were also examined using XRD measurements. From the integrated Pd/C and Pd/C/CNT patterns, the contributions from the carbon substrates were subtracted, and the resulting XRD profiles are shown in Figure 4. The XRD patterns were similar, and the major peaks were assigned to the metallic Pd.

3.2 XAFS: The concentration of Pd in the Pd/C and Pd/C/CNT samples

XAFS is a method able to determine the concentration of specific elements (absorbing atoms) for a relatively large volume. In this case, the weights of the Pd nanoparticles in a volume of 0.4 x 0.15 x 1 cm = 0.06 cm^3 were determined.

"An absolute absorption coefficient" was calculated by dividing the transmission XAFS spectra from samples by an empty spectrum recorded without any sample (the empty space between the first and second ionization chamber). Figure 5 shows the absolute absorption coefficients of the Pd/C and Pd/C/CNT samples and the absorption coefficient of a 20-μm-thick Pd reference foil.

The weights of the Pd nanoparticles in the illuminated volume, calculated from the heights of the absorption edges (edge jumps), were evaluated to be 0.38±0.03 mg and 0.27±0.03 mg for Pd/C and Pd/C/CNT, respectively. The Pd/C sample had approximately 29 wt. % more Pd than the Pd/C/CNT sample.

3.3 EXAFS signal analysis

To quantify the local atomic environment around Pd in the Pd/C and Pd/C/CNT samples, the corresponding EXAFS signal analysis was performed. The fitting of reference (known) sample datasets to an unknown structure is typical for EXAFS analysis for two main reasons:

(1) Fitting of signals for known structures provides information about a possible energy offset (a small shift of the measured data on the photon energy scale) and instrumental broadening. The instrumental broadening, which is a function of momentum (k), always convolutes with the sample signal and could strongly influence the determination of the coordination number; it must be accounted for in the experimental data [30].

(2) An estimation of the particular parameter errors is obtainable from the refinement of a known structure. In this manner, the maximum uncertainties in our data were estimated to be ±0.02 Å and ±1 atom for the interatomic distances and coordination numbers, respectively.

The normalized and k^2 weighted EXAFS data above the Pd *K* edge for the Pd/C and Pd/C/CNT samples and the reference foil are displayed in Figure 6a. It can be noted that the sinusoidal oscillations measured for Pd nanoparticles are very similar to the oscillations observed in the Pd reference sample but are different and locally greatly different (approximately 5.5 $Å^{-1}$) in amplitude.

Figure 6b shows the positive modulus of the Fourier transforms (*FT*s) for the corresponding EXAFS signals. The dominant peak visible in all spectra (located at approximately 2.5 Å) corresponds to the closest metal-metal (Pd-Pd) atomic pairs. The reduced height of this peak in Pd/C compared to Pd/C/CNT can be attributed to the smaller number of the metallic pairs, likely with a higher degree of disorder, indirectly leading to the conclusion that the Pd particles in Pd/C are smaller than those in Pd/C/CNT.

The nanoparticle signals at approximately 1.5 Å differ significantly from the reference foil. The peaks in this area were investigated due to the possibility of metal-carbon (Pd-C) pairs, but no relevant record of a Pd-C phase in crystallographic databases, such as ICDD PDF2 [31] or Pearson's Crystal Data [32], was found. However, Shawn et al. [33] reported a Pd-C interaction at approximately 3.6 Å in a 10% Pd/C catalyst prepared via $PdCl_2$ impregnation. Mojet et al. [34] also observed Pd–C coordination at r = 3.6 and 4.3 Å in fresh $Pd(NH_3)_4Cl_2$/C-fibrils and at r = 2.6 Å in reduced Pd/C-fibrils. Additionally, Chenov et al. [35] reported Pd–C shells at r = 2.3 and 3.3 Å in PdC_{60} prepared from an organometallic precursor. Jones et al. [36] reported Pd–C shells at r = 1.95 and 3.46 Å in $PdC_{0.15}$ powders, but McCaully [37,38] did not observe such Pd–C coordination in $PdC_{0.13}$. Our analysis confirms that the closest atomic shell coordinating Pd atom is located at approximately 1.99 Å, which is significantly shorter than the values reported above, except for those reported by Jones et al. [36]. Conversely, different types of oxides, such as PdO, Pd_2O, and PdO_2, could be formed. The shortest Pd-O distance, approximately 2 Å, is the same as the distance of the first atomic shell coordinating Pd atoms located at the particle surfaces, which will be shown later.

To obtain quantitative values for the structural parameters of the first two shells around Pd absorbing atoms, the shells were first isolated from the rest of the particle by applying a Hanning window followed by back Fourier transformation (*BFT*) to *k*-space. In the next step, the filtered

signals were numerically fit using the EXAFS formula (equations 1 and 2) based on the single scattering approximation [23]. It is important to emphasize that the EXAFS analysis of the Pd core and oxide layer on the top is very difficult due to the large number of free parameters (8 for the PdO layer and 4 for the first coordination shell of the nanoparticle metallic core) involved in the fitting procedure. An effective way to reduce this number is the application of additional constraints to the theoretical model, which, as a consequence, will also improve the stability of numerical fitting and reduce undesirable correlations. The applied constraints must have both physical and chemical sense, which requires some advance knowledge about the structure being investigated. Some constraints applied in our analysis used previously obtained knowledge, mainly from the diffraction results, while others reflect different types of overall assumption:

-for the metallic core, the interatomic distance, coordination number and square relative displacement (Debye–Waller factor) were constrained to values obtained from fitting the Pd reference foil EXAFS signal, $R_{Pd\text{-}Pd}$=2.729 Å, N=11.8 and σ^2= 0.005 Å^2.

-for the oxide surface layer, there are 2 shells (Pd-O and Pd-Pd) for which the Debye–Waller factor was constrained to be the same ($\sigma^2_{Pd\text{-}O} = \sigma^2_{Pd\text{-}Pd}$). Presumably, if one expects a strong chemical bond between Pd and O and a weaker bond between Pd and Pd, the σ^2 for Pd–O and Pd–Pd will be different. To support this constraint, it must be stated that it is impossible to precisely quantify the individual Pd–O and Pd–Pd σ^2 from the experiments performed. Therefore, these parameters need to be constrained to obtain a unique solution from the fitting. Therefore, the obtained σ^2 parameter from our analysis represents an overall atomic displacement, a term similar to B_{iso} used in X-ray powder diffraction.

The filtered back-Fourier transformed (*BFT*) and Fourier transformed (*FT*) signals of the Pd/C/CNT, together with the best theoretical fit (solid line), are shown in Figures 7a and 7b,

respectively. A visual examination of the plots revealed only moderate agreement between the experimentally obtained data and theoretically calculated results, which might be explained by a highly asymmetric (non-Gaussians) distribution of the back-scattering atoms as the sum of atoms located in the nanoparticle body and at the surface. In fact, EXAFS is very sensitive to the details of the distribution due to the high values of momentum transfer, Q = 2k, twice the value of a conventional diffraction experiment. There are two methods mostly used for better treatment of disorder effects. The first one assumes a physically reasonable shape for the non-Gaussian one-dimensional distribution and optimizes its parameters by comparing the experimental EXAFS to the theoretical model. Unfortunately, we did not have enough detailed information about the interatomic distribution for this approach. The second method, frequently used by the EXAFS community, is a model-independent approach based on the cumulative expansion of the EXAFS signal. This approach increases the number of free parameters by at least two and causes frequent problems with series convergence, and Freund [39] concluded that two additional parameters (C3 and C4) were not statistically justified for the first shell of a selection of metals, semiconductors and halides. For this reason, we were satisfied with the simple EXAFS formula, equations (1) and (2), quoted in the theoretical part of this work.

The structural parameters determined from the EXAFS signal analysis are listed in Table 1.

The information obtained from these result are as follows:

- the distance between Pd and O is 1.99 ± 0.02 Å, very close to the Pd-O distance of the tetragonal PdO phase, 2.011 Å [40]. In this phase, each Pd atom is coordinated by 4 O atoms, and the same value for the coordination number was obtained from our fit.

- in the tetragonal PdO phase, the second shell is composed of 4 Pd atoms separated from the central one by a distance of 3.02 Å. A very similar distance, but only for half of the atoms, was observed in our samples. The explanation could be as follows: only the Pd atoms located at the

particle surface are coordinated by 4 oxygen atoms, forming a PdO monolayer, while atoms in the second shell come from the interior metallic core. Because of the absence of a layer above Pd-O, the Pd-Pd coordination number is only half (N_{Pd-Pd}=2) of the value of a complete PdO unit cell. This explanation is schematically shown in Figure 8.

3.4 XANES signal analysis

Figure 9a shows the normalized X-ray-absorption near-edge structure (XANES) of the Pd/C and Pd/C/CNT samples measured at the Pd-*K* absorption edge together with the signal from the Pd reference foil. Visual examination of the plots reveals differences between the signals taken from the Pd/C and Pd/C/CNT samples. First, the onset of the Pd-*K* absorption edges of the Pd/C and Pd/C/CNT samples are slightly shifted towards higher photon energies compared with the reference foil signal. One of the possible explanations for this shift could be the presence of the Na_2PdCl_4 precursor in the experimental samples. However, the presence of this molecule is very unlikely after a 1 hour reduction in 10-11 pH solution. Moreover, no trace (emission) of chloride in the investigated samples was confirmed by SEM/EDX analysis. Therefore, the observed shift can be explained by the decrease of electron density around Pd atoms due to a charge transfer between Pd and O. In other words, smaller particles mean a proportionally higher number of oxidized surface sites in the investigated volume, which, on average, reduces the overall number of electrons around Pd in the sample. This loss of charge causes a "blue" shift of the nanoparticles signal to higher energies. The second difference is that the Pd/C signal above the edge is less structured (less pronounced peaks and valleys) than the Pd/C/CNT signal. A less-structured signal is a consequence of a higher static disorder originating from the smaller particle

dimensions (more grain boundaries in the investigated volume). This structural disorder can effectively suppress XANES resonances. Figure 9b shows the XANES signal from the Pd/C/CNT sample together with the FEFF 9.01 theoretically calculated absorption cross-sections of a Pd-O monolayer and an atomic cluster from an FCC Pd particle with a diameter of 6 Å. It is obvious that some features of the Pd/C/CNT signal can be represented by the metallic Pd, while other features can be represented by the metal oxide.

In the case of the presence of multiple phases in the sample under investigation, the XANES signal can be described as a linear combination of the theoretically calculated metallic Pd and PdO XANES signals. A quantitative measurement of the composition was obtained by finding the best linear combination of the calculated XANES spectra that fits the experimental spectra. The results of the linear combination fit for the Pd/C and Pd/C/CNT samples are shown in Figures 10a and 10b, respectively. From this analysis, the phase composition of the nanoparticles in the Pd/C sample was estimated to be 55% PdO and 45% Pd. Similarly, nanoparticles in the Pd/C/CNT sample consisted of 37.5% PdO and 62.5% Pd. It was mentioned previously that the oxides form a monolayer on top of the metallic body, so the ratio between PdO and Pd can also be observed as the ratio between the surface and the volume. Assuming a spherical shape for the particles (confirmed by the TEM images, Figure 1), the average particle diameter could be "naively" calculated from the following equation:

$$\frac{A}{V} = \frac{4\pi r^2}{\frac{4}{3}\pi r^3} = \frac{3}{r} \qquad (3)$$

where A is the surface areas, V is the volume and r is the particle radius. The diameter of the nanoparticles has been estimated to be 5 nm in the Pd/C sample and 10 nm in the Pd/C/CNT sample. The calculated sizes are actually very close to the values determined from the TEM

images (see Figure 3). Figure 11 shows the visualization of the nanoparticle metallic core, oxide monolayer and Pd-based nanoparticle with a diameter of 5 nm.

4 Conclusions

The aim of the present work was to report the synthesis and characterization of palladium - activated carbon Pd/C and palladium - activated carbon - multiwalled carbon nanotube Pd/C/CNT catalysts. The goal was to compare the structure of the catalysts prepared in the same way with the same metal content (3 wt. %) using two different supports.

- For the prepared catalysts, the specific surface area values were 692 $m^2 g^{-1}$ for Pd/C and 531 $m^2 g^{-1}$ for Pd/C/CNT. A decrease in the specific surface area of the prepared catalysts was observed because the palladium loaded onto the support caused pore blocking, which resulted in a decrease in the specific surface area of the prepared catalysts. In the case of Pd/C/CNT, the lower value of the SSA is also a consequence of the support material mixture.

- Transmission electron microscopy identified nanosized Pd-based particles with the space group Fm-3m in both samples. The particles in both samples exhibited nearly spherical morphologies but differences in size. The mean diameters of the particles in the Pd/C and Pd/C/CNT samples were estimated to be 5.4 nm and 7.8 nm, respectively.

- The nanoparticle phase composition was examined using XRD. The patterns from both the Pd/C and Pd/C/CNT samples are similar, and the major peaks were assigned to the metallic FCC-Pd phase.

- The weight of the Pd nanoparticles in a volume of 0.06 cm^3 was estimated to be 0.39±0.03 mg and 0.27±0.03 mg for the Pd/C and Pd/C/CNT samples, respectively. There is approximately 29 wt. % more Pd in the Pd/C sample than in the Pd/C/CNT sample.

- The EXAFS signal analysis proved the existence of Pd-Pd pairs in both samples, the same as in the metallic FCC Pd phase. In contrast to the pure Pd, Pd-O pairs originate from the nanoparticles surfaces as well. The Pd atoms at the particle surfaces are coordinated by 4 oxygen atoms to form a PdO monolayer covering an interior metallic core. Visualizations of these findings are shown in Figures 8 and 11.

- The XANES signals from the Pd/C and Pd/C/CNT show a shift of the absorption edge towards higher photon energies, showing an overall increase in the oxidation states of the Pd atoms in these samples. This shift is more pronounced for Pd/C, which indirectly indicates a smaller particle size in the Pd/C sample than in the Pd/C/CNT sample.

- The estimated phase composition of the nanoparticles in the Pd/C sample was 55% PdO and 45% Pd. The nanoparticles in the Pd/C/CNT sample consist of 37.5% PdO and 62.5% Pd. By allowing some assumptions (a Pd-O monolayer covering a Pd metallic core and only spherical samples), the diameter of the particles could be estimated to be 5 nm in the Pd/C sample and 10 nm in the Pd/C/CNT samples. The sizes obtained from spectroscopy are in good agreement with TEM observations.

Acknowledgments

This work was supported by the Ministry of Education, Science, Research and Sport of SR on behalf of the Agency of the Ministry of Education, Science, Research and Sport for EU structural funds, the project "Hydrogenation in liquid phase", ITMS project code 26220220144, Activity

2.1: Preparation and characterization of the support catalysts suitable for hydrogenation in the liquid phase, under the operational program Research and Development. K. S. is indebted to the Slovak Grant Agency for Science for financial support (Grant No. 2/0167/10)

References

[1] M.L.Toebes, J.A.van Dillen, K.P. de Jong, J. Mol. Catal. A: Chem. 173 (2001) 75-98.

[2] V.A. Semikolenov, Russian Chemical Reviews 61 (1992) 168-174.

[3] T. Harada, SH. Ikeda, M. Miyazaki, T. Sakata, H. Mori, M. Matsumura, J. Mol. Catal. A: Chem. 268 (2007) 59-64.

[4] N. Bouchenafa-Saıb, P. Grange, P. Verhasselt, F. Addoun, V. Dubois, Appl. Catal., A. 286 (2005) 67-174.

[5] E.A.Gelder, S.D. Jackson, C.M. Lok, Catal. Lett. 84 (2002) 205-208.

[6] L. Ma, Sh. Chen, CS. Lu, QF. Zhang, XN. Li, Catal. Today173 (2011) 62–67.

[7] Sh. Watanabe, V. Arunajatesan, Top. Catal. 53 (2010) 1150–1152.

[8] R.J. Kalbasi, N. Mosaddegh, J. Solid State Chem. 184 (2011) 3095-3103.

[9] LR. Kong, XF. Lu, XJ. Bian, WJ. Zhang, C. Wang, J. Solid State Chem.183 (2010) 2421-2425.

[10] M. Wang, DJ. Guo, HL. Li, J. Solid State Chem. 178 (2005) 1996-2000.

[11] A. Cabiac, G. Delahay, R. Durand, P. Trens, B. Coq, D. Plee, Carbon 45 (2007) 3–10.

[12] N. Bouchenafa-Saib, P. Grange, P. Verhasselt, F. Addoun, V. Dubois, Appl. Catal., A: Gen. 286 (2005) 167-174.

[13] H. Bazzazzadegan, M. Kazemeini, A.M. Rashidi, Appl. Catal., A: Gen. 399 (2011) 184-190.

[14] M.J. Ledoux, R. Vieira, C. Pham-Huu, N. Keller, J. Catal. 216 (2003) 333–342.

[15] C. Pham-Huu, N. Keller, G. Ehret, L.J. Charbonniere, R. Ziessel, M.J. Ledoux, J. Mol. Catal. A: Chem. 170 (2001) 155–163.

[16] P. Serp, M. Corrias, P. Kalck, Appl. Catal., A: Gen. 253 (2003) 337–358.

[17] A. Jung, A. Jess, T. Schubert, W. Schuetz, Appl. Catal., A: Gen. 362 (2009) 95-105.

[18] F. Salman, C. Park, R.T.K. Baker, Catal. Today 53 (1999) 385-394.

[19] AM. Zhang, JL. Dong, QH. Xu, XL. Li, Catal. Today 93-95 (2004) 347-352.

[20] R. Bouchard, D. Hupfeld, T. Lippmann, J. Neuefeind, H.B. Neumann, H.F. Poulsen, U. Rütt, T. Schmidt, J.R. Schneider, J. Süssenbach, M. von Zimmermann, J. Synchrotron Radiation 5 (1998) 90-101.

[21] A.P. Hammersley, S.O. Svensson, M. Hanfland, A.N. Fitch, D. Hausermann, High Press. Research 14 (1996) 235–248.

[22] J.J. Rehr, R.C. Albers, Rev. Mod. Phys. 72 (2000) 621-654.

[23] K.V. Klementev, J. Phys. D 34 (2001) 2241–2247.

[24] M. Benfatto, C.R. Natoli, A. Bianconi, J. Garcia, A. Marcelli, M. Fanfoni, I. Davoli, Phys. Rev. B 34 (1986) 5774-5781.

[25] J.J. Rehr, J.J. Kas, M.P. Prange, A.P. Sorini, Y. Takimoto, F. Vila, Comptes Rendus Physique 10 (2009) 548-559.

[26] M.J. Ward, P.A. Rupar, M.W. Murphy, Y.M. Yiu, K.M. Baines, T.K. Sham, Chem. Comm. 46 (2010) 7016-7018.

[27] J.E. Mueller, O. Jepsen, O.K. Andersen, J.W. Wilkins, Phys. Rev. Lett. 40 (1975) 720-722.

[28] A.L. Ankudinov, B. Ravel, J.J. Rehr, S.D. Conradson, Phys. Rev. B 58 (1998) 7565-7576.

[29] X.G. Zhang, A. Gonis, Phys. Rev. Lett. 62 (1989) 1161-1164.

[30] B.K. Teo, EXAFS: Basic Principles and Data Analysis; Springer, Berlin, 1986.

[31] JCPDS-International Centre for Diffraction Data, ICDD. & J.C.P.D.S.- International Center for Diffraction Data., version 2.0, 1997.

[32] P. Villars, K. Cenzual, Pearson's Crystal Data: Crystal Structure Database for Inorganic Compounds (on CD-ROM), Release 2012/13, ASM International®, Materials Park, Ohio, USA

[33] D.L. Shawn, H. Yin-Hou, J. Po-Hau, L. Jyh-Fu, J. Mol. Catal. A: Chemical 238 (2005) 88–95.

[34] B.L. Mojet, M.S. Hoogenraad, A.J. van Dillen, J.W. Geus, D.C. Koningsberger, J. Chem. Soc., Faraday Trans. 93 (1997) 4371-4375.

[35] V.A. Chenov, V.N. Ivanova, A.N. Kozhevikova, G.A. Mardezhova, S.G. Nikitenko, A.A. Nikiforov, Nucl. Instrum. Methods Phys. Res. A 359 (1995) 250-253.

[36] D.J. Jones, J. Roziere, L.E. Aleandri, B. Bogdanovic, S.C. Huckett, Chem. Mater. 4 (1992) 620-625.

[37] J.A. McCaully, Phys. Rev. B 47 (1993) 4873-4879.

[38] J.A. McCaully, Phys. Rev. B 48 (1993) 666.

[39] Freund, J. Phys. Lett. A 157 (1991) 256-260.

[40] J.M. Walter, P.J. Linus, J. Am. Chem. Soc.63 (1941) 1392–1394.

Table 1. Structural parameters of Pd-based nanoparticles in the Pd/C/CNT sample determined from the Pd-K edge EXAFS spectra analysis.

C-B* pair	$r_{C\text{-}B} \pm 0.02$Å[Å]	$N_B \pm 1$ atom	σ^2 [Å2]	ΔE [eV]
Pd-O nanoparticle surface	1.99	4	0.004	8.06
Pd-Pd nanoparticle core	2.73	12	0.005	3.9
Pd-Pd nanoparticle surface	3.05	2	0.004	-2.2

* C–B means central–back-scattered atoms

Figure Captions

Figure 1. TEM images of the Pd nanosized particles in the specimen a) Pd/C; b) Pd/C/CNT.

Figure 2.Marked SAED patterns corresponding to pure metallic Pd in the specimen a) Pd/C; b) Pd/C/CNT.

Figure 3. Histogram of the Pd particles size distribution.

Figure 4. XRD patterns of the Pd/C and the Pd/C/CNT specimens after subtraction of corresponding carbon support signals.

Figure 5. Absolute absorption coefficient of the Pd/C (black curve), Pd/C/CNT (green curve) and 20μm thick Pd reference foil (blue dashed line).

Figure 6. a) Normalized and k^2 weighted EXAFS data of the Pd/C (black), Pd/C/CNT (green) samples and Pd reference foil (blue dashed curve) measured above the Pd K edge, b) possitive Fourier transforms (FTs) modulus of corresponding EXAFS signals.

Figure 7. EXAFS spectra analysis of the Pd/C/CNT sample a) back Fourier transforms of first three shells around Pd absorbing atoms (open circles) together with fitted model (solid red line), b) Fourier transforms (open circles) of normalized experimental EXAFS spectra shown together with model (solid red line).

Figure 8. Visualisation of atoms arrangement at the nanoparticle surface. Pd atoms are represented by grey balls and oxygen atoms by the red balls. Pd atoms in FCC unit cells (nanoparticle metallic core) are connected by lines. On the top of them is one of possible Pd-O monolayer structure.

Figure 9. a) Normalized X-ray-absorption near-edge structure (XANES) of the Pd/C (black), Pd/C/CNT (green) and the Pd reference foil (blue) measured at Pd-K absorption edge, b) XANES signal from the Pd/C/CNT sample shown together with FEFF 9.01 theoretically calculated absorption cross-sections from Pd-O monolayer (red) and atomic cluster from fcc Pd of diameter 6Å (orange curve).

Figure 10. Normalized X-ray-absorption near-edge structure (XANES) of the Pd/C a) and Pd/C/CNT b) (open circles). The lines are fits using a linear combination of the reference spectra shown in Fig. 9b.

Figure 11. Visualization of metallic core (left), oxide monolayer (middle) and nanoparticle of diameter 5nm (right).

Graphical abstract legand

Visualization of metallic core (left), oxide monolayer (middle) and nanoparticle of diameter 5 nm (right).

Highlights

- Pd catalysts were prepared on two types of supports: carbon and carbon nanotubes.
- BET, TEM, XRD characterization of prepared catalysts.
- XAFS: Concentration of Pd in samples Pd/C and Pd/C/CNT
- EXAFS and XANES signal analysis of catalysts.
- Visualisation of atoms arrangement at the Pd nanoparticle surface.

List of Figures:

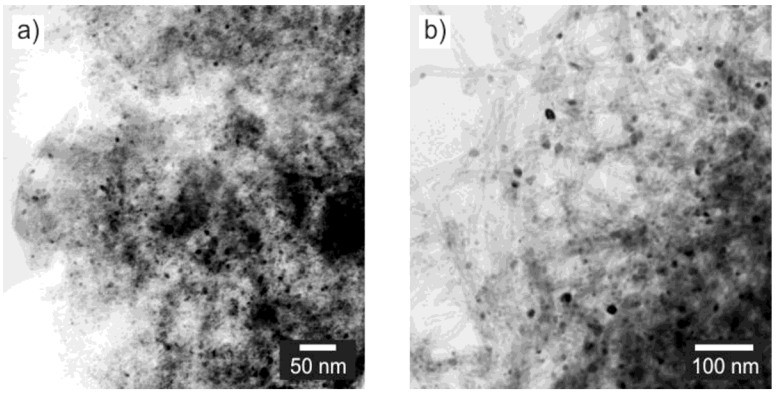

Figure 1.

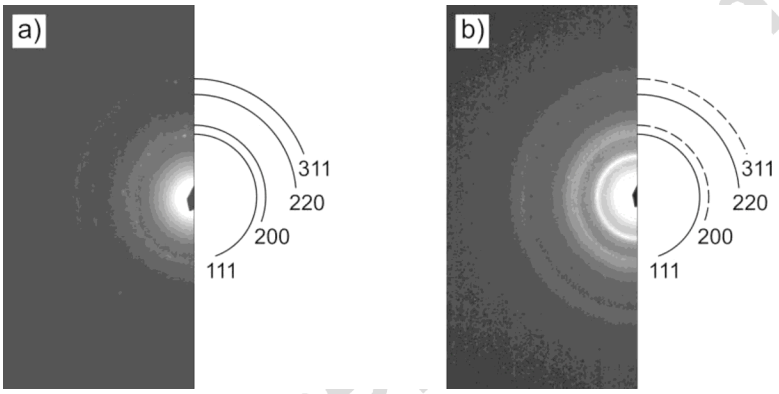

Figure 2.

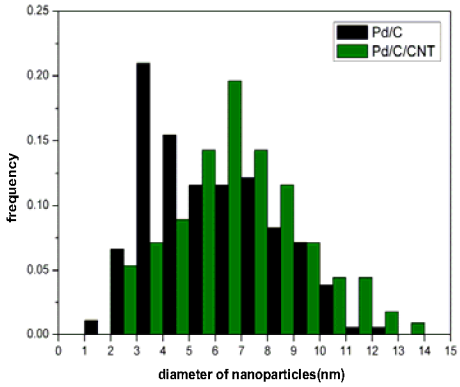

Figure 3.

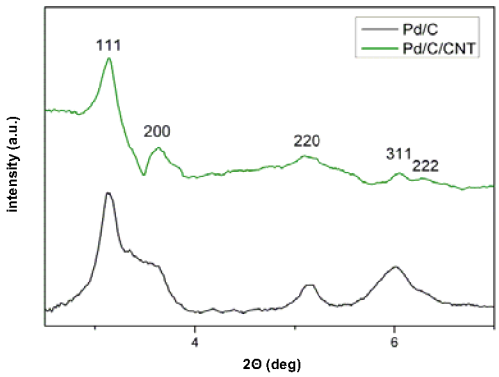

Figure 4.

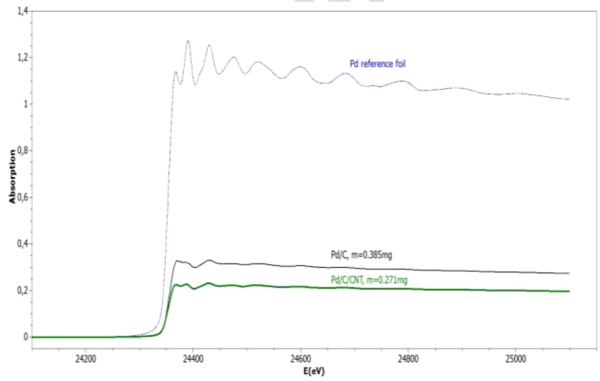

Figure 5.

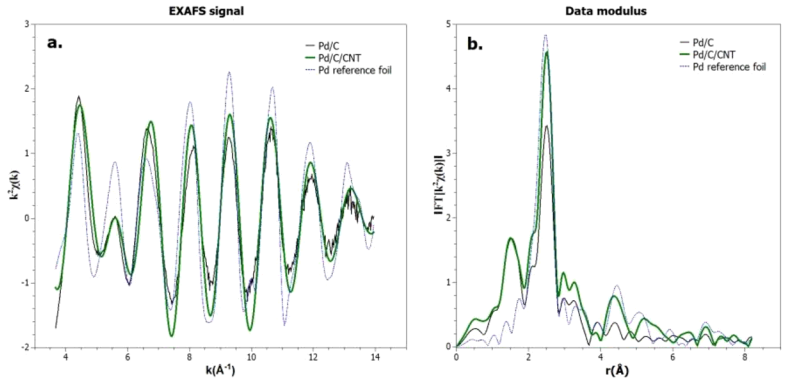

Figure 6.

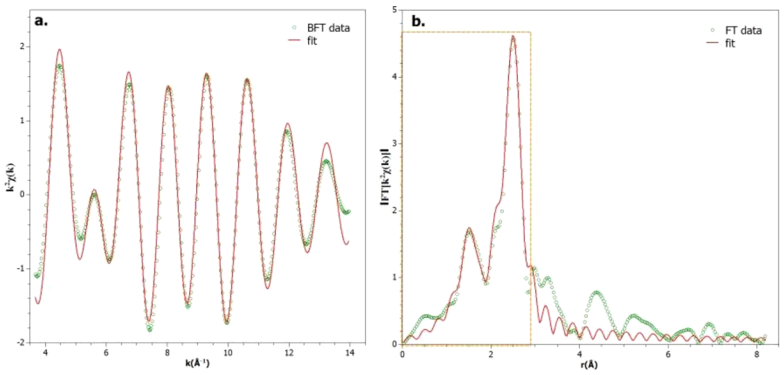

Figure 7.

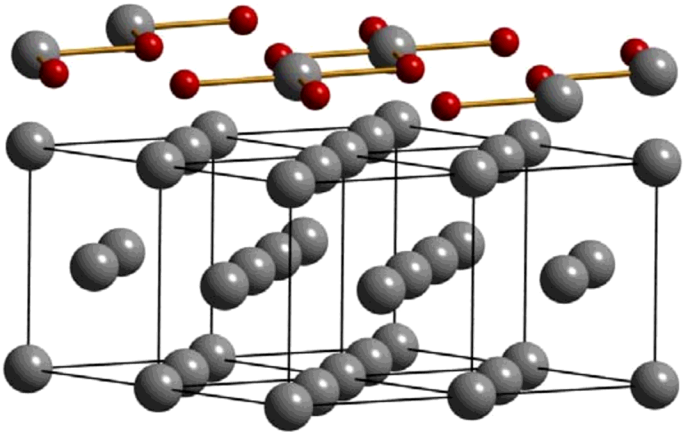

Figure 8.

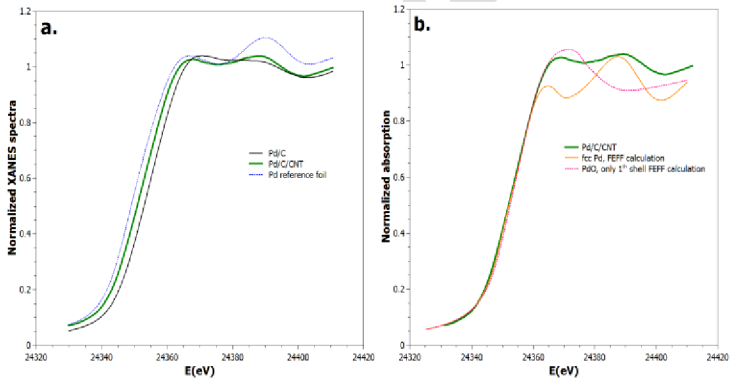

Figure 9.

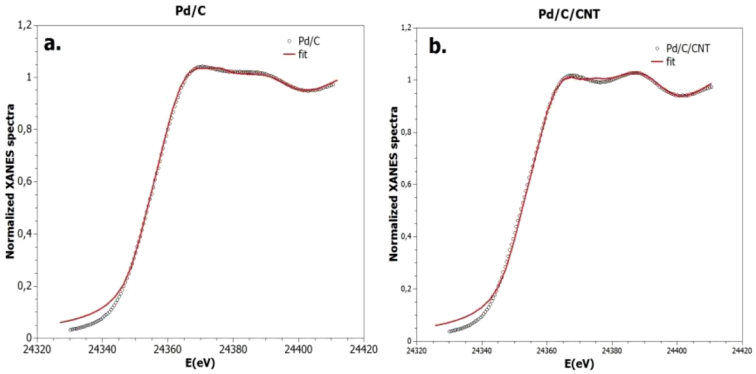

Figure 10.

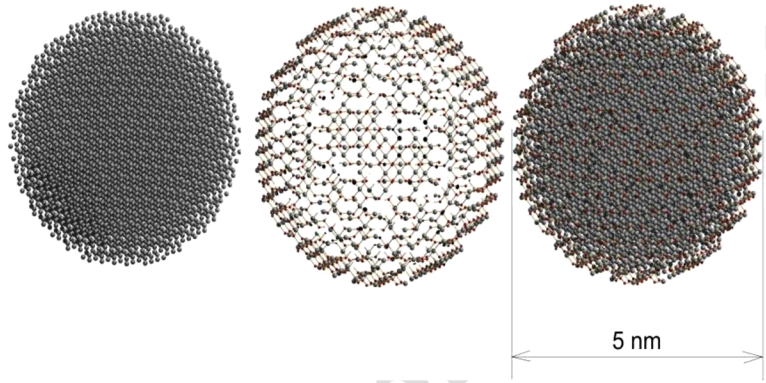

Figure 11.

*Graphical Abstract (TOC Figure)